Asian Journal of Pharmaceutical Sciences 19 (2024) 100955

Available online at www.sciencedirect.com

ScienceDirect

journal homepage: www.elsevier.com/locate/AJPS

Research Article

Deep near infrared light-excited stable synergistic photodynamic and photothermal therapies based on P-IR890 nano-photosensitizer constructed *via* a non-cyanine dye

Dawei Jiang[a,b,c,d,1], *Chao Chen*[e,f,1], *Peng Dai*[a,c,d,1], *Caiyan Li*[a,c,d], *Zhiyi Feng*[a,c,d], *Na Dong*[a,c,d], *Fenzan Wu*[a,c,d], *Junpeng Xu*[a,c,d], *Ping Wu*[a,c,d], *Liuxi Chu*[a,c], *Shengcun Li*[c,d,g], *Xiaokun Li*[c,d,h,*], *Youjun Yang*[i,*], *Weian Zhang*[b,*], *Zhouguang Wang*[a,c,d,h,*]

[a] *Affiliated Cixi Hospital, Wenzhou Medical University, Ningbo 325300, China*
[b] *Shanghai Key Laboratory of Functional Materials Chemistry, School of Materials Science and Engineering, East China University of Science and Technology, Shanghai 200237, China*
[c] *School of Pharmaceutical Science, Wenzhou Medical University, Wenzhou 325000, China*
[d] *Oujiang Laboratory, Zhejiang Lab for Regenerative Medicine, Vision and Brain Health, School of Pharmaceutical Science, Wenzhou 325000, China*
[e] *Institute for Environmental Pollution and Health, School of Environmental and Chemical Engineering, Shanghai University, Shanghai 200444, China*
[f] *Shanghai Key Laboratory of Chemical Biology, School of Pharmacy, East China University of Science and Technology, Shanghai 200237, China*
[g] *Rehabilitation Medicine Center, The Second Affiliated Hospital and Yuying Children's Hospital of Wenzhou Medical University, Wenzhou 325000, China*
[h] *National Key laboratory of macromolecular drug development and manufacturing, School of Pharmaceutical Science, Wenzhou Medical University 325035, China*
[i] *State Key Laboratory of Bioreactor Engineering, Biomedical Nanotechnology Center, Shanghai Collaborative Innovation Center for Biomanufacturing Technology, School of Biotechnology, East China University of Science and Technology, Shanghai 200237, China*

ARTICLE INFO

Article history:
Received 13 April 2024
Revised 20 June 2024
Accepted 1 July 2024
Available online 24 August 2024

ABSTRACT

The cyanine dyes represented by IR780 can achieve synergistic photodynamic therapy (PDT) and photothermal therapy (PTT) under the stimulation of near-infrared (NIR) light (commonly 808 nm). Unfortunately, the stability of NIR-excited cyanine dyes is not satisfactory. These cyanine dyes can be attacked by self-generated reactive oxygen species (ROS) during PDT processes, resulting in structural damage and rapid degradation, which is fatal for phototherapy. To address this issue, a novel non-cyanine dye (IR890) was elaborately designed and synthesized by our team. The maximum absorption wavelength of IR890 was located in the deep NIR region (*ca.* 890 nm), which was beneficial for further improving

* Corresponding authors.
E-mail addresses: xiaokunli@wmu.edu.cn (X. Li), youjunyang@ecust.edu.cn (Y. Yang), wazhang@ecust.edu.cn (W. Zhang), wzhouguang@gmail.com (Z. Wang).
[1] These authors contributed equally to this work.
Peer review under responsibility of Shenyang Pharmaceutical University.

https://doi.org/10.1016/j.ajps.2024.100955

Keywords:
Photodynamic therapy
Photothermal therapy
IR780
Non-cyanine dye
Deep near infrared light

tissue penetration depth. Importantly, IR890 exhibited good stability when continuously illuminated by deep NIR light. To improve the hydrophilicity and biocompatibility, the hydrophobic IR890 dye was grafted onto the side chain of hydrophilic polymer (POEGMA-b-PGMA-g-C≡CH) *via* click chemistry. Then, the synthesized POEGMA-*b*-PGMA-*g*-IR890 amphiphilic polymer was utilized to prepare P-IR890 nano-photosensitizer *via* self-assembly method. Under irradiation with deep NIR light (850 nm, 0.5 W/cm^2, 10 min), the dye degradation rate of P-IR890 was less than 5%. However, IR780 was almost completely degraded with the same light output power density and irradiation duration. In addition, P-IR890 could stably generate a large number of ROS and heat at the same time. It was rarely reported that the stable synergistic combination therapy of PDT and PTT could be efficiently performed by a single photosensitizer *via* irradiation with deep NIR light. P-IR890 exhibited favorable anti-tumor outcomes through apoptosis pathway. Therefore, the P-IR890 could provide a new insight into the design of photosensitizers and new opportunities for synergistic combination therapy of PDT and PTT.

1. Introduction

Photodynamic therapy (PDT) is gaining increasing attention as a clinical cancer therapeutic due to negligible side effects, favorable therapeutic efficiencies and easy spatiotemporal operations [1-5]. Under light irradiation with a specific wavelength, the photosensitizer interacts with oxygen to generate highly biologically toxic ROS, which causes the oxidation of biological macromolecules (proteins, nucleic acids, lipids, etc.) and subsequently results in cancer cell apoptosis and death [6-9]. Based on the above PDT mechanism, photosensitizer is a key factor that determines the excitation wavelength and ROS production efficiency. An ideal photosensitizer should have good biocompatibility, great ROS production efficiency, and excellent stability under continuous light illumination. In addition, the excitation wavelength of photosensitizer should be longer, which is beneficial for increasing tissue penetration depth [10,11]. Conventional organic and inorganic photosensitizers utilized in cancer therapy include porphyrin, phthalocyanine, chlorin, cyanine, methylene blue, BODIPY, metallic oxides, semiconductors, metal nanoparticles, etc. [12-17]. The excitation wavelengths for these photosensitizers are mostly located in ultraviolet (UV) and visible regions. The tissue penetration depth for UV light is limited, and long-term exposure to UV light can cause serious side effects such as skin damage. In order to enhance the depth of tissue penetration and reduce the side effects, near-infrared (NIR) light-excited photosensitizers are more attractive. Remarkably, partial cyanine dyes represented by IR780 can achieve high PDT efficiency under excitation with NIR light (commonly 808 nm) [18-25]. Due to their increased tissue penetration depth and good ROS production efficiency, the NIR light-excited cyanine dyes have become attractive photosensitizers for PDT. It is meaningful to design and develop new photosensitizers that can be excited with longer light wavelength, preferably longer than 808 nm, in order to enhance tissue penetration depth further and reduce the side effects.

The rapid growth of malignant tumors leads to increased demand for oxygen and glucose, while the blood supply in tumor tissues is relatively insufficient [26-28]. Due to lacking blood supply, tumor easily forms hypoxic microenvironment. The PDT therapeutic effect will be significantly reduced in such a hypoxic environment [29-31]. In order to improve therapeutic effect, PDT is often combined with chemotherapy, immunological therapy, photothermal therapy (PTT) and other treatments [32-35]. PTT involves converting light into heat, which increases the local temperature and causes cancer cell death [36,37]. The increased local temperature is helpful in enhancing the blood supply of tumor tissue and relieving tumor hypoxia, which can improve PDT efficacy [38-40]. Furthermore, PTT is oxygen-independent and does not affect the treatment effect for hypoxic tumors in theory. However, the efficiency of a single PTT treatment is often limited. This can be ascribed to the rapid expression of heat shock proteins, which elevates the heat tolerance of tumor and thus reduces the therapeutic effect [41-44]. Hence, the combination of PTT and PDT can overcome the limitations of single treatment modes and synergistically improve the anticancer therapeutic effect.

To combine PDT and PTT, different kinds of photodynamic reagents and photothermal reagents are commonly integrated together [45-47]. Notably, partial cyanine dyes, such as IR780, can realize synergistic therapy of PDT and PTT through a single photosensitizer [48-52]. This synergistic combination of PDT and PTT based on a single photosensitizer can simplify the composition of functional biomaterials and reduce the complexity of the production process, making them more advantageous for practical applications in cell, animal and clinical experiments. Unfortunately, the stability of NIR-excited cyanine dyes is not satisfactory. These cyanine dyes can be attacked by self-generated ROS during PDT processes, resulting in structural damage and unsustainable photodynamic and photothermal processes [53-55]. Therefore, it has significant scientific research value and great practical clinical translational potential for designing and developing new photosensitizers with good stability, high tissue penetration depth, and excellent

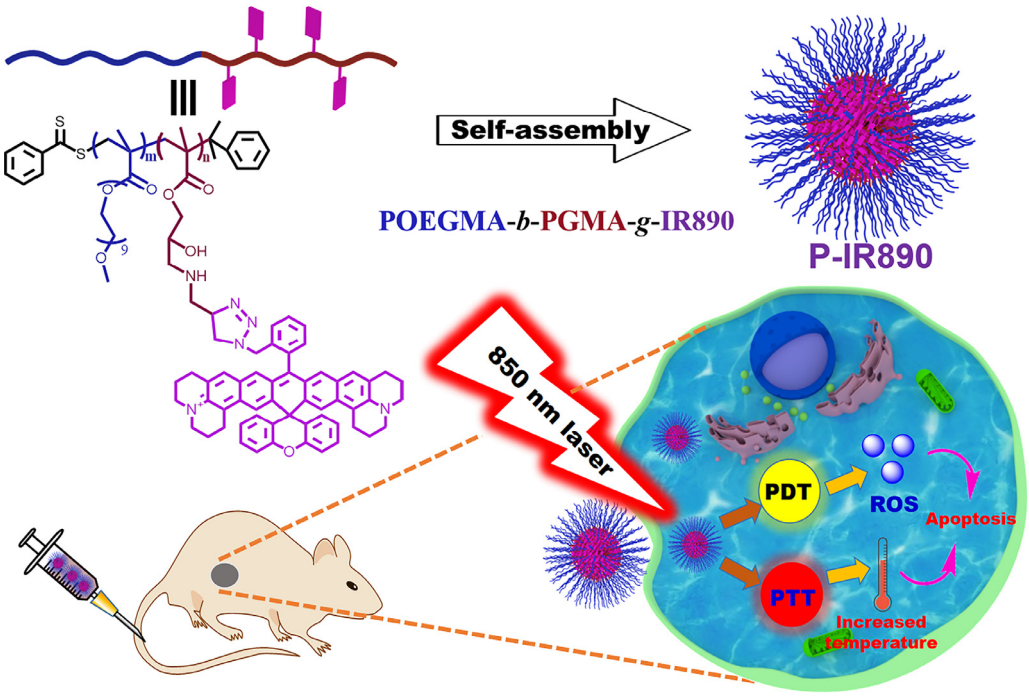

Scheme 1 – Schematic illustration for preparation of P-IR890 nano-photosensitizer *via* self-assembling of amphiphilic polymer (POEGMA-*b*-PGMA-*g*-IR890) in aqueous solution. Under irradiation of a 850 nm laser, P-IR890 could induce synergistic treatment of PDT and PTT to induce apoptosis of cancer cells.

synergistic combination of PTT and PDT *via* only one kind of photosensitizer.

Herein, we prepared a nano-photosensitizer (abbreviated as P-IR890), which was constructed by self-assembly of a non-cyanine dye (IR890) grafted amphiphilic polymer for deep NIR light-excited stable synergistic photodynamic and photothermal therapies. Briefly, the organic small molecule dye of IR890 has good stability and a strong absorption peak in the deep NIR region around 890 nm, which has been clearly reported in our previous work [56]. Then, the hydrophobic IR890 was grafted onto the side chains of POEGMA-*b*-PGMA-*g*-C≡CH polymers *via* click chemistry. The POEGMA segment of POEGMA-*b*-PGMA-*g*-C≡CH has good hydrophilicity, biocompatibility and low immunogenicity, which has been widely used in studies for anti-tumor therapies [57,58]. In addition, chemically grafted IR890 could reduce or avoid early drug leakage during blood circulation compared with simple physical embedding. Then, IR890 grafted amphiphilic block polymer (POEGMA-*b*-PGMA-*g*-IR890) was obtained and characterized. Subsequently, the P-IR890 nano-photosensitizer was prepared through self-assembly of POEGMA-*b*-PGMA-*g*-IR890 in aqueous solution. Under irradiation of an 850 nm laser, P-IR890 has good photothermal conversion behavior to conduct PTT. In addition, P-IR890 can interact with ambient oxygen to generate a large amount of ROS for PDT (Scheme 1). In this work, the ROS detection assay was conducted to evaluate the photodynamic behavior of P-IR890. The photothermal conversion behavior and photo-stability of P-IR890 were also evaluated. 4T1 cancer cells were used to evaluate the intracellular ROS production, the biocompatibility and phototoxicity of P-IR890, respectively. Apoptosis assays for 4T1 cells induced by P-IR890 were also conducted. Finally, a nude mouse model of xenograft 4T1 tumor was used to test the synergistic therapeutic effect of PDT and PTT under excitation with deep NIR light *in vivo*. The results demonstrated the promising potential of P-IR890 as a highly efficient and stable nano-photosensitizer for deep NIR light excited synergistic photodynamic and photothermal therapies. These findings may have significant implications for the development of new cancer treatment strategies.

2. Materials and methods

2.1. Materials

OEGMA (Mn = 480), AIBN, copper(I) bromide, glycidyl methacylate (GMA), PMDETA, anhydrous diethyl ether, propargylamine, dichloromethane (DCM), triethylamine (TEA), and tetrahydrofuran (THF) were bought from Sigma-Aldrich and used directly. 1, 3-diphenylisobenzofuran (DPBF), chloroform-d ($CDCl_3$), 2′,7′-dichlorodihydrofluorescein diacetate (DCFH-DA), N,N-dimethylformamide (DMF), and RAFT chain transfer agent (2-Phenyl-2-propylbenzodithiolate, CDB) were purchased from Aladdin and used directly.

2.2. Characterization

^{1}H NMR spectra were measured using a spectrophotometer (BRUKER AV400, 400 MHz), employing $CDCl_3$ as solvent and tetramethylsilane as internal reference. Dynamic light

scattering (abbreviated as DLS) was detected with a Zetasizer Nano ZS instrument. TEM images were captured using an electron microscope (JEOL JEM1400). UV–vis spectra were acquired with a UV-2450 UV-visible spectrophotometer. Confocal laser scanning microscopy (abbreviated as CLSM) studies were conducted on a Nikon A1R. For photothermal detection, Fluke Ti27 infrared thermal camera was utilized.

2.3. Synthesis of POEGMA polymer

The POEGMA polymer was synthesized *via* RAFT polymerization. In brief, OEGMA (2.08 mmol, 1 g), AIBN (0.053 mmol, 8.746 mg) and CDB (0.16 mmol, 43.584 mg) were dissolved in 4 ml THF and added into Schlenk flask. After degassed with freeze vacuum-thaw cycles, the mixture solution was heated at 65 °C for 12 h. Afterwards, the reaction mixture was precipitated in cold diethyl ether to remove unreacted OEGMA. Then, the obtained viscous POEGMA was dried in a vacuum oven at 25 °C for 48 h.

2.4. Synthesis of POEGMA-*b*-PGMA diblock polymer

POEGMA was used as a macromolecular chain transfer agent to polymerize GMA also *via* RAFT polymerization in order to obtain POEGMA-*b*-PGMA. POEGMA (500 mg), GMA (150 mg), AIBN (3 mg), and THF (6 ml) were added into Schlenk flask with a magnetic stirring bar. After undergoing three freeze-thaw cycles, the above mixed solution was sealed under vacuum and subsequently immersed in an oil bath at 65 °C. The polymerization process was halted after a duration of 24 h. In the final step, the reaction solution was precipitated in cold diethyl ether to remove any residual GMA. The resultant POEGMA-b-PGMA was left to vacuum drying at 25 °C for 24 h.

2.5. Synthesis of POEGMA-*b*-PGMA-*g*-IR890 block polymer

POEGMA-*b*-PGMA (200 mg), propargylamine (100 mg), TEA (20 mg), and THF (6 ml) were added into Schlenk flask. After reacting at room temperature (RT) for 48 h, the reaction solution was precipitated with cold diethyl for many times to remove unreacted propargylamine. The resultant product was vacuum-dried at RT for 24 h for subsequent use.

To synthesize the POEGMA-*b*-PGMA-*g*-IR890 block polymer, the obtained product (30 mg), PMDETA (3 mg) and IR890 (15 mg) were dissolved in 5 ml DMF. Under protection of argon gas, 4 mg CuBr was added to the mixture. Then, the above solution was stirred at 65 °C for 24 h. Subsequently, the reaction mixture was passed through a neutral alumina column to eliminate copper catalysts and was dialyzed against H_2O to remove PMDETA and organic solvent. The final POEGMA-*b*-PGMA-*g*-IR890 block polymer was obtained by lyophilizing.

2.6. Preparation of P-IR890 nano-photosensitizer

The P-IR890 nano-photosensitizer was readily prepared by nanodeposition method. Briefly, 5 mg POEGMA-*b*-PGMA-*g*-IR890 block polymer was dissolved in 1 ml of DMSO and slowly added dropwise into 4 ml water with intense stirring. The solution was vigorously stirred for another 2 h and dialyzed against H_2O to totally remove the organic solvent (MWCO = 3,500). The concentration of grafted IR890 in the obtained P-IR890 nanoparticles aqueous solution was determined with the standard curve (Fig. S1).

2.7. Photo-stability detection

Firstly, P-IR890 solution was detected with a UV-2450 UV-visible spectrophotometer to acquire UV-visible absorption spectra. After that, the above solution in quartz cuvette was irradiated with an 850 nm laser (0.5 W/cm^2) for 10 min. The UV–Vis absorption spectra of the illuminated solutions were subsequently tested again under the same conditions. The photo-stability of IR780 was detected with the similar method, but irradiated with a 808 nm laser (0.5 W/cm^2, 10 min).

2.8. NIR laser-induced temperature increase forP-IR890

To evaluate the photothermal effect of the P-IR890 nano-photosensitizer, 500 µl P-IR890 solution with different concentrations of IR890 (5, 10, 20, 50 µg/ml) was separately added into 1.5 ml EP tube. These tubes were then exposed to an 850 nm laser (0.5 W/cm^2) for 180 s. The temperature change was recorded using Fluke Ti27 thermal imaging camera. The control group was treated with 500 µl PBS.

2.9. ROS detection

DPBF was utilized to detect ROS. To enhance solubility, DPBF was prepared with 1% DMSO and added to 3 ml of P-IR890 solution. The solution was subsequently irradiated with an 850 nm laser (0.5 W/cm^2). The DPBF decay at 420 nm was monitored at intervals of either 5 or 10 s using a UV–vis spectrophotometer.

2.10. Cell culture

Dulbecco's modified Eagle's medium (DMEM) containing 10% fetal bovine serum (FBS) and penicillin/streptomycin (100 U/ml each) was utilized for culturing 4T1 cancer cells. Cultures were maintained under a humidified atmosphere containing 5% CO_2 at 37 °C.

2.11. ROS detection in cancer cells

The production of intracellular ROS was ascertained using DCFH-DA *via* CLSM. Intracellularly, DCFH-DA undergoes deacetylation by esterases, yielding -DCFH. Upon exposure to ROS, DCFH converts to fluorescent dichlorofluorescein (DCF). 4T1 cells were plated onto glass-bottomed petri dishes. Following a 24-h incubation, the cells were co-cultured with either PBS, IR890 or P-IR890 (10 µg/ml of free IR890) for an additional 24 h. The above cells were washed and incubated with DCFH-DA for another 30 min. Subsequent to another thorough wash with PBS, cells were irradiated with a laser (850 nm, 0.5 W/cm^2, 5 min). The DCF fluorescence was subsequently examined by CLSM.

2.12. In vitro *toxicity assessment*

4T1 cells were cultured with a density of 5,000 cells per well. The free IR890 or P-IR890, suspended in culture medium at varying concentrations, was added to the wells. After incubation for 1 d, cells were rinsed with sterilized PBS and irradiated with a laser (850 nm, 0.5 W/cm^2, 10 min) for phototoxicity detection or in the dark for dark-toxicity detection. Then MTT was used according to the operation instructions. Cell viability was determined using the formula:

$$\text{Cell viability (\%)} = \left(OD_{test} - OD_{background}\right)/\left(OD_{control} - OD_{background}\right) \times 100\%.$$

2.13. *Live/dead staining assay*

Incubated with free IR890 or P-IR890 for 12 h, the 4T1 cells were washed with PBS. Then, the treated cells were either exposed or not exposed to an 850 nm laser (0.5 W/cm^2, 10 min). Finally, the cancer cells were analyzed by an inverted fluorescent microscope (Axio Observer 7) with Calcein/PI staining kit.

2.14. *Cell apoptosis analysis*

4T1 cells were seeded in 6-well plates (2×10^5 cells/well) overnight, then the cells were incubated with PBS or P-IR890 for 12 h. Subsequently, the above cells were cultured in the dark or irradiated with an 850 nm laser (0.5 W/cm^2, 5 min). The above-treated cells were harvested and determined by flow cytometry using AnnexinV-FITC/PI Apoptosis Kit.

2.15. *Western blot (WB) analysis*

The P-IR890 or PBS-treated 4T1 cells were subjected to irradiation using an 850 nm laser at a power density of 0.5 W/cm^2 for 5 min or left untreated. Following an additional 4-h incubation, the treated cells were washed with ice-cold PBS and then lysed using 300 μl extract buffer for 30 min on ice. The proteins present in the cell lysate were separated on a 10% SDS-PAGE gel and subsequently transferred onto PVDF membranes. These membranes were then exposed to a blocking buffer for 1 h at room temperature and incubated overnight with anti-cleaved Caspase-3, anti-Bcl-2, and anti-Bax antibodies. Afterward, the membranes were stained with corresponding secondary antibodies for 1 h at room temperature. The visualization of protein bands was carried out using a ChemiDoc XRS+ Chemiluminescence gel imager manufactured by BIO-RAD, located in the USA.

2.16. *Xenograft tumor mouse model*

All animal procedures were compliant with the National Institutes of Health Guide for the Care and Use of Laboratory Animals and received approval from the Scientific Investigation Board of Oujiang Laboratory (NO: OJLAB24020103). The xenografted tumor mouse models were established by subcutaneous injection of 4T1 cells (1×10^7) into the flanks of female BALB/c nude mice (6–8 weeks old). The volume of the tumors was estimated by the equation:

$$\text{Volume} = (\text{Tumor Length}) \times (\text{Tumor Width})^2/2.$$

2.17. In vivo *photothermal evaluation*

In vivo photothermal evaluation was performed by intravenously administering the P-IR890 nano-photosensitizer to tumor-bearing nude mice at a dose of 5 mg/kg of free IR890. After 24-h administration, tumor tissues were exposed to an 850 nm laser (0.5 W/cm^2) for 4 min. The temperature change of the mice body was monitored using a Fluke Ti27 infrared thermal imaging camera.

2.18. In vivo *tumor growth inhibition*

Once the tumor size reached 100–200 mm^3, the mice were divided into four groups randomly, with each group consisting of four mice. Subsequently, the mice received a tail vein injection of either 100 μl PBS, IR890 or P-IR890 (10 mg/kg of free IR890). After 24 h post-injection, the tumors were subjected to irradiation using an 850 nm laser at a power density of 0.5 W/cm^2 for 10 min, or they were kept in the dark. The tumor volume and body weight of each mouse were recorded every 2 d. At Day 14, the mice were euthanized, and the tumors were collected and weighed. Key organs and the tumors were obtained for histological examination using H&E staining.

2.19. *Statistical analysis*

Experimental data are exhibited as mean ± standard deviation (SD). The one-way ANOVA was employed to ascertain statistical significance, which was considered at $P < 0.05$.

3. Results and discussion

3.1. *Synthesis and characterization of POEGMA-b-PGMA-g-IR890 block copolymer*

The IR890 grafted amphiphilic block copolymer (POEGMA-*b*-PGMA-*g*-IR890) was synthesized in four steps. The detailed synthetic route is shown in Fig. 1A. First, POEGMA was synthesized by RAFT polymerization. According to the ^{1}H NMR spectrum (Fig. 1B), the average degree of polymerization of OEGMA was 17. Subsequently, the obtained POEGMA was used as a macromolecular chain transfer agent to further polymerize glycidyl methacrylate (GMA) monomer to obtain POEGMA-*b*-PGMA block polymer (Fig. 1C). Next, alkynyl group was grafted onto the side chain of the polymer *via* the ring-opening reaction of propargylamine and epoxypropane group. The structure of the obtained POEGMA-*b*-PGMA-g-C≡CH was confirmed by ^{1}H NMR spectrum. As shown in Fig. S2, the characteristic peak appeared at 1.78 ppm ascribed to **H**C≡C– of propargylamine. Finally, amphiphilic POEGMA-*b*-PGMA-*g*-IR890 block polymer was prepared through "click chemistry" reaction between the alkynyl group of POEGMA-*b*-PGMA-g-C≡CH and azide group of IR890. The successful grafting of IR890 was confirmed by the appearance of characteristic

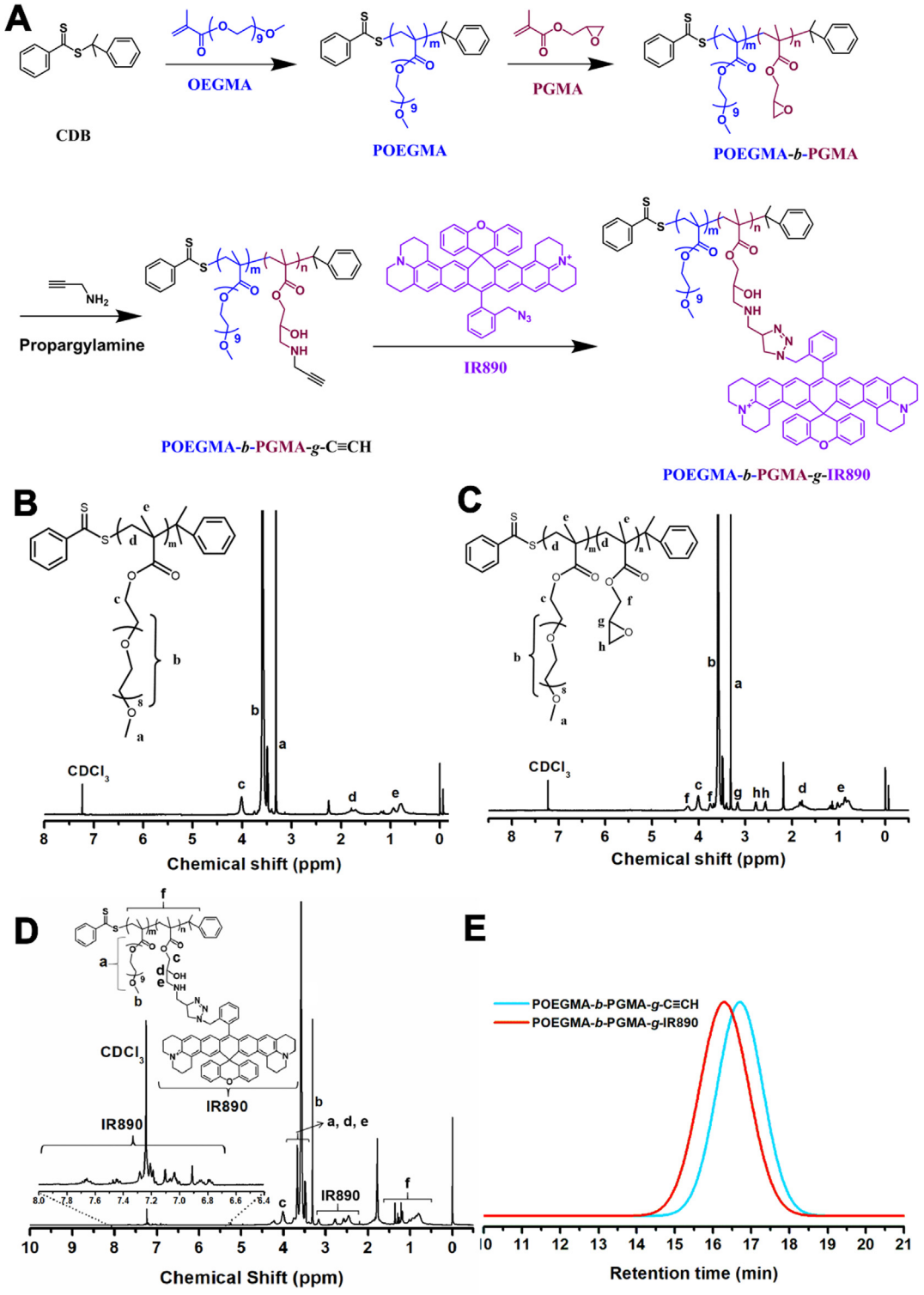

Fig. 1 – Synthesis and characterization of POEGMA-*b*-PGMA-*g*-IR890 block polymer. (A) The synthetic route of POEGMA-*b*-PGMA-*g*-IR890. (B) ^{1}H NMR of POEGMA. (C) ^{1}H NMR of POEGMA-*b*-PGMA. (D) ^{1}H NMR of POEGMA-*b*-PGMA-*g*-IR890. (E) The GPC traces of POEGMA-*b*-PGMA-*g*-C≡CH and POEGMA-*b*-PGMA-*g*-IR890.

peaks of hydrogen protons at low field (8–6.5 ppm) attributed to grafted IR890 in the ^{1}H NMR spectrum (Figs. 1D and S3). The average grafting rate of IR890 was calculated to be about 82%, and the molecular weight was about 19,837 daltons. According to the gel permeation chromatography (GPC) traces (Fig. 1E), the retention time of POEGMA-*b*-PGMA-*g*-IR890 decreased from 17.72 min for POEMA-b-PGMA-g-C≡CH polymer to 16.28 min, due to the increased weight-average molecular weight (M_w), which also confirmed the successful grafting of IR890 on the polymer.

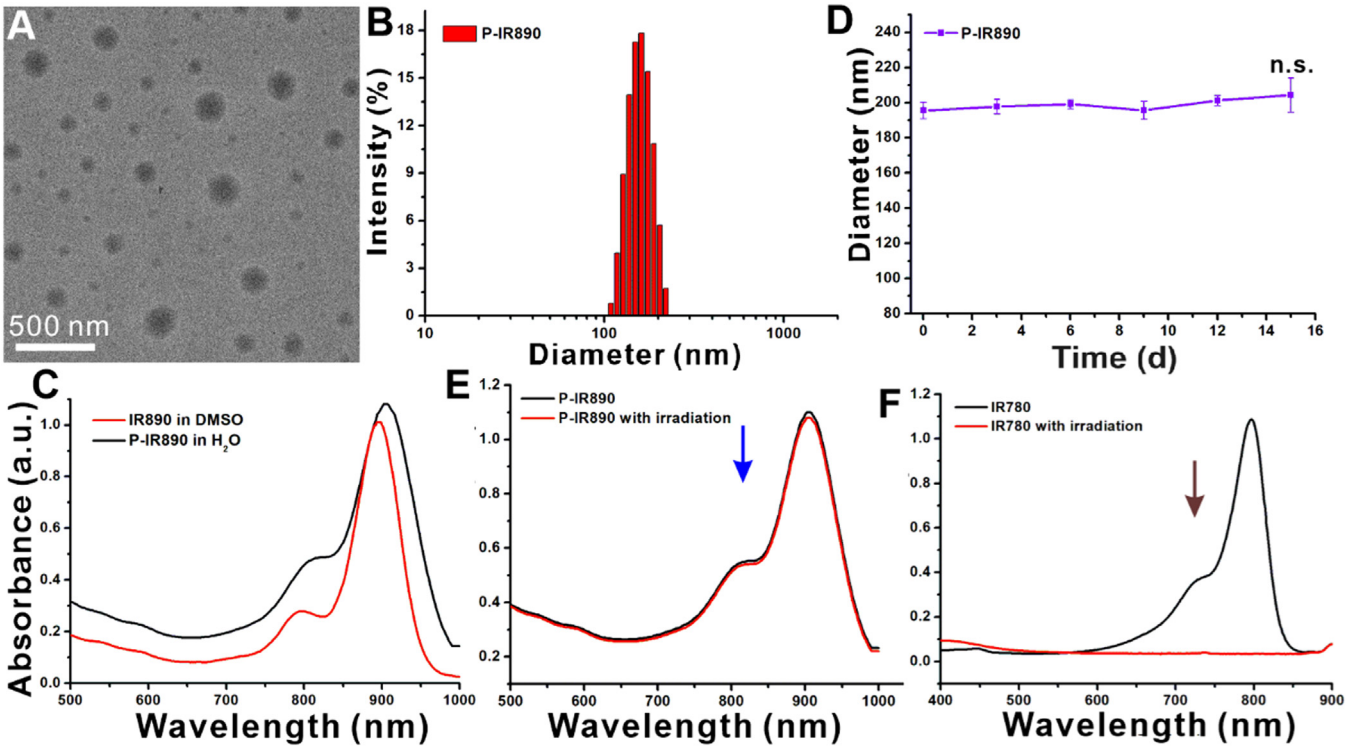

Fig. 2 – Preparation and characterization of P-IR890 nano-photosensitizer. (A) The TEM image of P-IR890. (B) DLS results of P-IR890 in PBS. (C) The UV–vis absorption spectra of IR890 and P-IR890. (D) The stability results of P-IR890. (E) The results of the photo-stability test for P-IR890. (F) The results of the photo-stability test for IR780.

3.2. *Preparation and characterization of P-IR890 nano-photosensitizer*

The P-IR890 nano-photosensitizer was prepared by self-assembly of POEGMA-*b*-PGMA-*g*-IR890 polymer in aqueous solution. The morphology of P-IR890 was detected by TEM, which revealed that P-IR890 has the spherical morphology (Fig. 2A). According to the dynamic light scattering (DLS) data (Fig. 2B), the hydrodynamic diameter of P-IR890 was about 196.4 nm. The polydispersity index (PDI) of P-IR890 was 0.15, which indicates a narrow size distribution. As shown in Fig. 2C, the maximum absorption peak of free IR890 dye in DMSO was located at about 890 nm. However, the maximum absorption peak of P-IR890 was red-shifted to 906 nm. This typical phenomenon could be attributed to the aggregation of grafted IR890 in the core of P-IR890 nanoparticles, which also conformed to the successful preparation of P-IR890 nano-photosensitizer. Furthermore, the size of P-IR890 varied slightly for two weeks (Fig. 2D), which indicated that the P-IR890 had good stability in PBS. In addition, P-IR890 also maintained nice stability in DMEM and FBS for at least 48 h (Fig. S4). The photostability of P-IR890 was subsequently detected. When P-IR890 was irradiated with an 850 nm laser (0.5 W/cm^2) for 10 min, the absorbance of P-IR890 barely decreased (Fig. 2E). The dye degradation rate of P-IR890 was calculated to be less than 5%. However, under the same light output power density and irradiation duration, the commercial cyanine dye (IR780) was almost completely degraded (Fig. 2F). These results clearly indicated that P-IR890 had good photostability for continuous phototherapy.

3.3. *Reactive oxygen species and photothermal detection* in vitro

The photodynamic and photothermal behaviors of P-IR890 were investigated under irradiation with an 850 nm laser (0.5 W/cm^2). Firstly, the photodynamic behavior of P-IR890 was investigated using DPBF. As a classical ROS detection reagent, the chemical structure of DPBF could be damaged by ROS, resulting in a decrease of the characteristic absorption peak at 420 nm. When the PBS group was irradiated with an 850 nm laser, almost no decrease was found for the characteristic absorption peak of DPBF (Fig. 3A). For the free IR890 group, the characteristic peak of DPBF at 420 nm gradually decreased under laser irradiation (Fig. S5). However, it is thrilling to find that the absorption peak of DPBF rapidly decreased for P-IR890 group under the same irradiation conditions (Fig. 3B). As shown in Fig. 3C, the relative absorbance of DPBF at 420 nm for PBS group exhibited negligible change by extension of irradiation time. However, the relative absorbance for P-IR890 group decreased more faster than IR890 group. These results clearly indicated that P-IR890 nano-photosensitizer could efficiently generate a large number of ROS under irradiation with deep NIR light.

The photothermal conversion behavior of P-IR890 in aqueous solution was subsequently investigated. When the illumination duration extended from 0 s to 180 s, the increased temperature of blank control group was less than 3 °C. Under the same illumination condition, P-IR890 nano-photosensitizer with different concentrations (5, 10, 20 and 50 μg/ml, respectively) all induced temperature enhancement

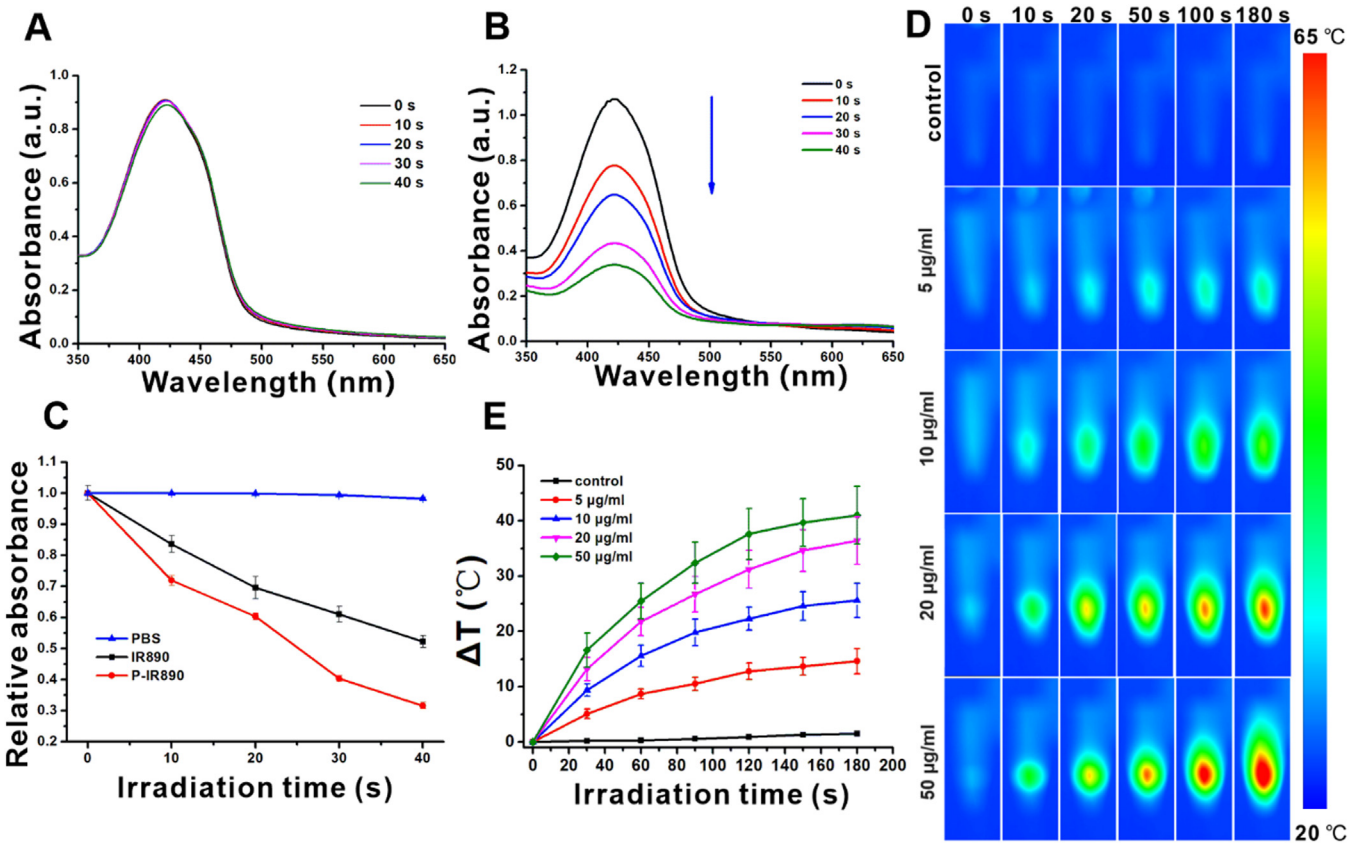

Fig. 3 – ROS and photothermal detection for P-IR890. (A) The ROS detection with DPBF for PBS group under irradiation of a 850 nm laser. (B) The ROS detection with DPBF for P-IR890 group under irradiation of a 850 nm laser. (C) The variation of relative absorbance at 420 nm for PBS group, IR890 group and P-IR890 group. (D) Thermal images recorded from P-IR890 with different concentrations. (E) The corresponding heating curve for D.

(Fig. 3D). The maximum solution temperature reached up to 63 °C. In addition, the temperature of the sample solution rose more rapidly with higher P-IR890 concentrations (Fig. 3E). According to photothermal cycling tests (Fig. S6), it could be found that P-IR890 could undergo at least 5 cycles. The photothermal conversion efficiency of P-IR890 was approximately 23.7%. It is interesting that P-IR890 exhibited a faster temperature increase and achieved a higher balanced temperature compared with free IR890 under the same dye concentration and laser output power (Fig. S7). This could be ascribed to the following reasons. Free IR890 was a highly hydrophobic molecule. However, P-IR890 possessed good dispersibility in aqueous solution, which enhanced their interaction with light so as to improve PTT effects. These results clearly indicated that P-IR890 nano-photosensitizer possessed good photothermal conversion ability.

The above ROS detection and photothermal detection results indicated that P-IR890 nano-photosensitizer could produce ROS and simultaneously generate heat under irradiation with an 850 nm laser. Therefore, the P-IR890 nano-photosensitizer (one stone) exhibited great potential for stable synergistic treatment of PDT and PTT (two birds) with excitation of deep NIR light, enabling a "one stone two birds" approach.

3.4. *ROS detection in cancer cells*

Intracellular ROS detection was performed using DCFH-DA, which was commonly used to detect intracellular ROS. After reacting with intracellular ROS, DCFH-DA was oxidized to generate DCF with strong green fluorescence. As shown in Fig. 4A, under irradiation of an 850 nm laser, the 4T1 cells for PBS group exhibited barely green fluorescence. For IR890 group, the treated 4T1 cells showed weak green fluorescence, indicating that a little ROS was produced. However, it was found that the 4T1 cells incubated with P-IR890 exhibited strong green fluorescence under the same detection conditions, indicating that P-IR890 could be taken up by cancer cells and efficiently generate a large amount of intracellular ROS. Overall, the intracellular ROS detection results further confirmed the potential of P-IR890 as a nano-photosensitizer for use in synergistic photodynamic and photothermal therapy.

3.5. *Cytotoxicity assay*

MTT assay was utilized to evaluate the cytocompatibility and phototoxicity of P-IR890 nano-photosensitizer against 4T1 cancer cells. According to MTT results (Fig. 4B), the

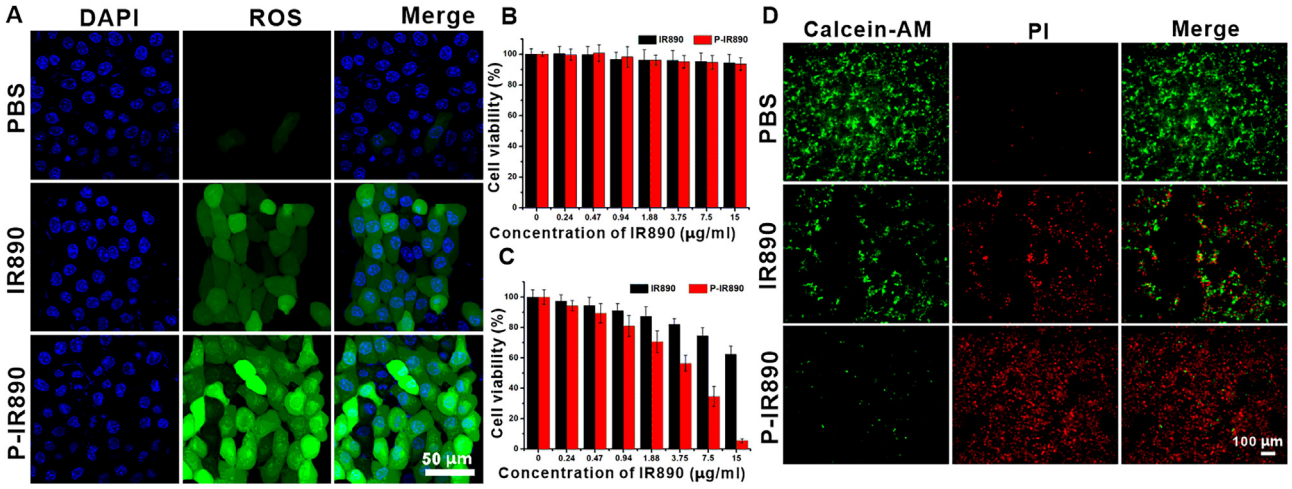

Fig. 4 – *In vitro* anti-tumor evaluation. (A) Intracellular ROS detection for 4T1 cells treated with PBS, IR890 or P-IR890 by using DCFH-DA probe. The nucleus of treated cancer cells were stained with DAPI. (Scale bar: 50 μm) (B) Cell viability of 4T1 cells treated with varying concentrations of IR890 or P-IR890 without light irradiation. (C) Cell viability of 4T1 cells treated with varying concentrations of IR890 or P-IR890 and irradiated with deep NIR light.(D) Live/dead staining images for 4T1 cells with different treatments. (Scale bar: 100 μm).

viability of 4T1 cells incubated with free IR890 or P-IR890 nano-photosensitizers with different concentrations (0–15 μg/ml of IR890) all above 90%. The LD50 of P-IR890 was measured to be about 18.54 mg/ml (Fig. S8). In addition, the hemolysis rates of IR890 and P-IR890 were all lower than 5% (Fig. S9). This indicated that P-IR890 has favorable cytocompatibility and hemocompatibility in the dark. Subsequently, the phototoxicity of P-IR890 nano-photosensitizer against 4T1 cancer cells was conducted. As shown in Fig. 4C, the cell viability of 4T1 cells treated with IR890 and P-IR890 gradually decreases with the enhancement of IR890 concentration. However, the decline in cell viability for the P-IR890 group is more pronounced with the increase in drug concentration. Especially when the concentration of IR-890 was 15 μg/ml, the cell viability for free IR890 group was about 65%, while the cell survival rate dropped to about 5% for the P-IR890 group, This significantly enhanced phototoxicity could be attributed to the increased production of ROS and heat within the cancer cells caused by P-IR890.

3.6. *Live/dead staining*

In order to further confirm the phototoxicity of P-IR890 for cancer cells, the live/dead staining assays were also conducted. Living cells could be stained by Calcein-AM with green fluorescence, while dead cells could be stained by PI with red fluorescence. As exhibited in Fig. 4D, the majority of 4T1 cells for PBS group showed strong green fluorescence. For IR890 group, the green fluorescence signal was diminishing, while the red fluorescence was intensifying. This indicated that a portion of the 4T1 cells treated with IR890 had undergone death. However, under an 850 nm laser irradiation, the green fluorescence significantly decreased. Meanwhile, a large number of red spots appeared for P-IR890 group. These results also confirmed that P-IR890 could efficiently kill cancer cells by synergistic interaction of PDT and PTT under light irradiation.

3.7. *Apoptosis detection*

Subsequently, Annexin V-FITC/PI apoptosis assays were carried out to explore the capability of P-IR890 nano-photosensitizer in inducing apoptosis by flow cytometry. As shown in Fig. 5A, apoptosis rate (Q2+Q3) for the PBS group and PBS+850 nm group was only 3.70% and 4.15%, respectively. The 4T1 cancer cells incubated with P-IR890 but without laser irradiation also exhibited a very low apoptosis rate (2.19% for late-stage and 2.98% for early stage). However, the apoptosis rate was significantly elevated to 35% for P-IR890+850 nm group. The obvious apoptosis induced by P-IR890+850 nm group was further verified by WB experiments. As exhibited in Fig. 5B and 5C, the levels of pro-apoptotic proteins (Bax) prominently increased for P-IR890+850 nm group compared with other groups. The cleaved Caspase-3 protein was also elevated for P-IR890+850 nm group. Meanwhile, the level of anti-apoptotic protein (Bcl-2) obviously decreased for P-IR890+850 nm group. These results suggested that ROS and heat generated from P-IR890 under the stimulation of deep near-infrared light could significantly induce cancer cell apoptosis.

3.8. In vivo *distribution and pharmacokinetics*

The *in vivo* distribution of P-IR890 was investigated by an IVIS fluorescence imaging system. After P-IR890 was tail intravenously injected in the mice, the fluorescence signal at the tumor sites gradually increased with the extension of injection time and arrived at a peak about 24 h postinjection (Fig. 6A). Then, the fluorescence intensity

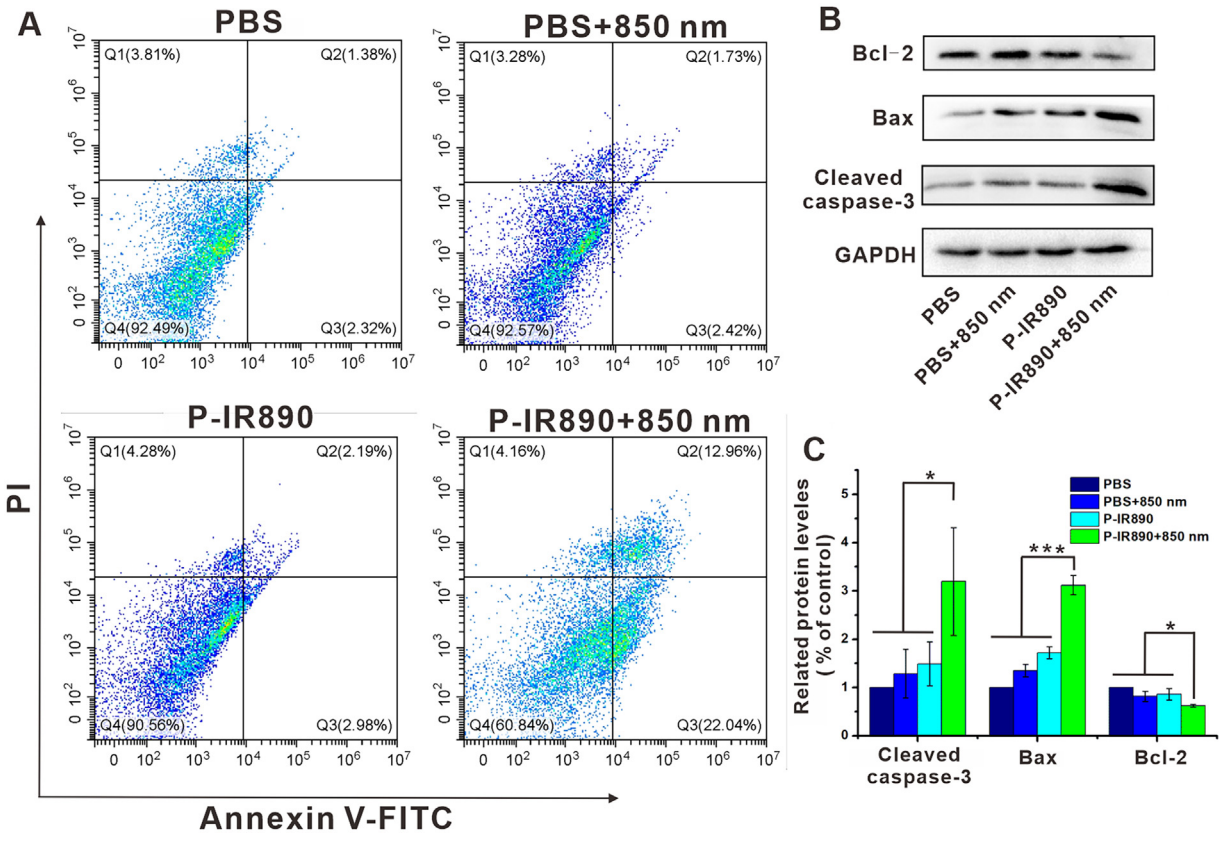

Fig. 5 – Apoptosis detection. (A) Flow cytometry assay on apoptosis of 4T1 cells with different treatments. (B) The protein expression levels of Bcl-2, Bax, and Cleaved caspase-3 in 4T1 cells after different treatments. (C) Semiquantitative evaluation of the expression level of these proteins. *P < 0.05, ***P < 0.001.

slowly decreased. After 72 h postinjection, the fluorescence signal at tumor site still remained strong. The *ex vivo* fluorescence images obtained at 72 h postinjection also exhibited strong fluorescence signals for the tumor (Fig. S10). These results indicated that P-IR890 could efficiently target the tumor sites, which could be ascribed to the enhanced permeability and retention (EPR) effect. Furthermore, the *in vivo* pharmacokinetics of P-IR890 was also detected. As shown in Fig. S11, P-IR890 was cleared in plasma with a half-life of about 2 h.

3.9. In vivo *photothermal imaging*

An infrared thermal imaging system was used to evaluate the *in vivo* photothermal behavior of P-IR890. After the P-IR890 nano-photosensitizer (5 mg/kg or 10 mg/kg) was tail intravenous injected into nude mouse for 24 h, the temperature of xenograft 4T1 tumor site increased obviously under irradiation with an 850 nm laser (Fig. 6B). It also could be found that the temperature of tumor site increased more by enhancing the injected concentration of P-IR890. However, the tumor temperature of PBS group only increased a little (< 3 °C) under the same experimental condition. According to the corresponding increasing temperature curve (Fig. 6C), the maximum elevated temperature of the tumor site was about 17 °C under irradiation with an 850 nm laser for 4 min. The above photothermal data indicated that P-IR890 could enrich at tumor site and perform good photothermal conversion behavior under irradiation of deep NIR light. In general, the *in vivo* photothermal imaging results demonstrated the potential of P-IR890 as a promising nano-photosensitizer for PTT.

3.10. In vivo *anti-tumor evaluation of P-IR890 nano-photosensitizer*

To evaluate the synergistic treatment of PDT and PTT using P-IR890 nano-photosensitizer, mice with xenograft 4T1 tumors were utilized. The mice with tumor volume of 100–200 mm^3 were randomly divided into 6 groups, each with four mice. The groups were named PBS, PBS+850 nm, IR890, IR890+850 nm, P-IR890 and P-IR890+850 nm, respectively. The mice in each group were injected with 100 μl PBS, IR890 or P-IR890 (10 mg/kg of IR890) by tail intravenous injection. After 24 h, each mouse in the PBS+850 nm group, IR890+850 nm and P-IR890+850 nm group was irradiated with an 850 nm laser (0.5 W/cm^2) for 10 min at the tumor site. The mice in the other groups were not illuminated. Subsequently, the tumor size and the weight of the mice were monitored every 2 d during the treatment. As shown in Fig. 6D, the tumor growth curves for the PBS group, PBS+850 nm group, IR890 and P-IR890 group exhibited similar trends, indicating that

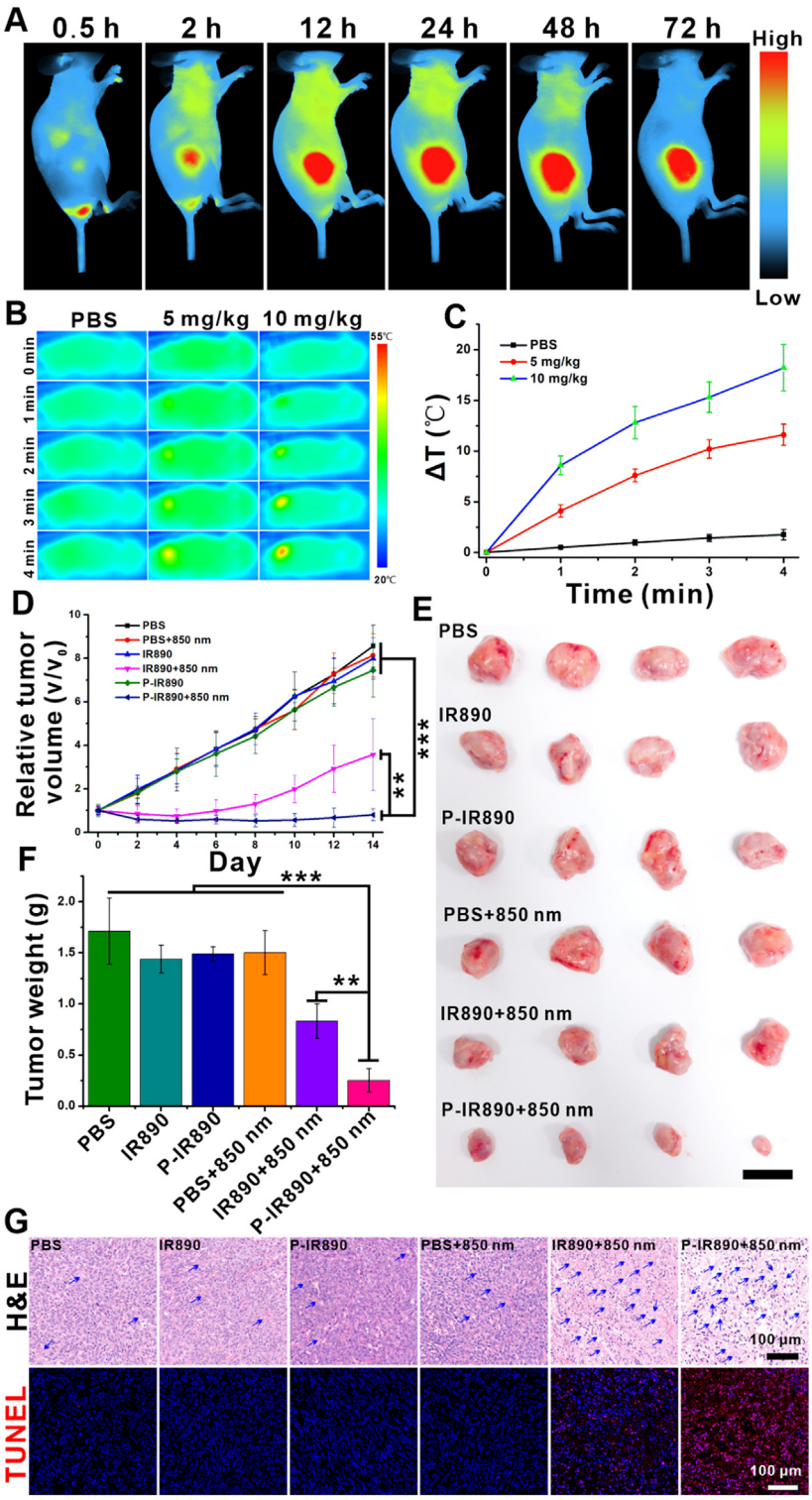

Fig. 6 – *In vivo* anti-tumor evaluation. (A) The *in vivo* distribution of P-IR890. (B) Thermal images of 4T1 tumor bearing mice with different treatments. (C) The corresponding increasing temperature curve for treated mice. (D) Growth curves of 4T1 tumors for different groups. (E) Photographs of tumors with different treatments on Day 14. (scale bar: 1 cm) (F) The corresponding average tumor weight with different groups on Day 14. (G) Representative images of H&E and TUNEL stained tumor sections from each treated group. The blue arrows indicated the necrosis of cancer cells. (Scale bar: 100 μm). $^{**}P < 0.01$, $^{***}P < 0.001$. (For interpretation of the references to colour in this figure legend, the reader is referred to the web version of this article.)

IR890 and P-IR890 could not suppress the tumor growth in the absence of light. Compared with PBS group, tumor growth was slowed for the IR890+850 nm group. However, the growth of the tumor volume for the P-IR890+850 nm group was severely inhibited, and the average tumor volume on Day 14 of P-IR890+850 nm group was about one-eleventh of the PBS group. The anti-tumor activity of P-IR890+850 nm treatment was further confirmed by intuitive photographs of excised tumors on Day 14. As shown in Fig. 6E, the excised solid tumor for P-IR890+850 nm group was the smallest. The corresponding average tumor weights on Day 14 also exhibited the lightest for P-IR890+850 nm group (Fig. 6F). In order to further verify the therapeutic effect of P-IR890 nano-photosensitizer, tumor slices for each group were stained with hematoxylin and eosin (H&E) and TUNEL. As shown in Fig. 6G, the P-IR890+850 nm group revealed significant damage compared with other groups, suggesting that P-IR890 nano-photosensitizer induced severe apoptosis and necrosis under irradiation with an 850 nm laser. During treatment, the weight of mice in each group was not significantly reduced, indicating that P-IR890 nano-photosensitizer has no obvious biological toxicity (Fig. S12). According to the slices of main organs (liver, heart, spleen, kidney and lung), there were negligible lesions to main organs for each group, indicating that P-IR890 nano-photosensitizer possessed good biological safety (Fig. S13). Hence, the *in vivo* anti-tumor evaluation of P-IR890 nano-photosensitizer demonstrated its potential as a promising strategy for the combined treatment of cancer using photodynamic and photothermal therapy.

4. Conclusion

In summary, a novel P-IR890 nano-photosensitizer was successfully designed and synthesized for stable synergistic combination therapy of PDT and PTT. Firstly, the non-cyanine IR890 dye with favorable photostability was grafted onto the side chain of a hydrophilic and biocompatible polymer, resulting in the formation of the amphiphilic POEGMA-*b*-PGMA-*g*-IR890 block polymer. Then, P-IR890 nano-photosensitizer was successfully prepared by self-assembly of POEGMA-*b*-PGMA-*g*-IR890 polymer in an aqueous solution. Maximum absorption peak of P-IR890 was located at the deep NIR region (about 906 nm). ROS detection results showed that P-IR890 could efficiently generate a large amount of ROS under excitation with an 850 nm laser. Photothermal detection results exhibited that P-IR890 could induce the rapid increase of local temperature under irradiation with deep NIR light. *In vitro* and *in vivo* assays exhibited that the P-IR890 had good biocompatibility in the absence of light. Under irradiation of an 850 nm laser, P-IR890 nano-photosensitizer could efficiently kill cancer cells and significantly inhibit tumor growth based on the synergistic treatment of PDT and PTT. Overall, these findings suggested that P-IR890 nano-photosensitizer could provide new insight into the design of photosensitizers for synergistic combination therapy of PDT and PTT and has the potential to be translated into practical applications for cancer therapy.

Conflicts of interest

The authors declare no competing financial interests in this paper.

CRediT authorship contribution statement

Dawei Jiang: Writing – original draft, Project administration, Methodology, Investigation, Funding acquisition. **Chao Chen:** Resources, Methodology, Investigation. **Peng Dai:** Validation, Methodology. **Caiyan Li:** Methodology, Data curation. **Zhiyi Feng:** Visualization, Formal analysis, Data curation. **Na Dong:** Formal analysis, Data curation. **Fenzan Wu:** Visualization, Formal analysis. **Junpeng Xu:** Visualization, Formal analysis. **Ping Wu:** Resources, Formal analysis. **Liuxi Chu:** Visualization. **Shengcun Li:** Visualization, Resources. **Xiaokun Li:** Writing – review & editing. **Youjun Yang:** Writing – review & editing, Resources, Investigation, Conceptualization. **Weian Zhang:** Writing – review & editing, Resources, Project administration, Investigation, Conceptualization. **Zhouguang Wang:** Writing – review & editing, Resources, Funding acquisition, Conceptualization.

Acknowledgements

This project was supported by National Natural Science Foundation of China (Grant No. 82271629 and 82301790), Leading Innovative and Entrepreneur Team Introduction Program of Zhejiang (Grant No. 2023R01002) and Ningbo Natural Science Foundation (Grant No. 2023J054).

Supplementary materials

Supplementary material associated with this article can be found, in the online version, at doi:10.1016/j.ajps.2024.100955.

References

[1] Hu JJ, Lei Q, Zhang XZ. Recent advances in photonanomedicines for enhanced cancer photodynamic therapy. Prog Mater Sci 2020;114:100685.
[2] Ivanova VA, Verenikina EV, Nikitina VP, Zhenilo OE, Kruze PA, Nikitin IS, et al. Photodynamic therapy for preinvasive cervical cancer. J Clin Oncol 2020;38:6035.
[3] Li X, Lovell JF, Yoon J, Chen X. Clinical development and potential of photothermal and photodynamic therapies for cancer. Nat Rev Clin Oncol 2020;17:657–74.
[4] Pham TC, Nguyen V-N, Choi Y, Lee S, Yoon J. Recent strategies to develop innovative photosensitizers for enhanced photodynamic therapy. Chem Rev 2021;121:13454–619.
[5] Li X, Chen L, Huang M, Zeng S, Zheng J, Peng S, et al. Innovative strategies for photodynamic therapy against hypoxic tumor. Asian J Pharm Sci 2023;18:100775.
[6] De Siqueira LBD, Matos APDS, Feuser PE, Machado-De-Avila RA, Santos-Oliveira R, Ricci-Junior E. Encapsulation of photosensitizer in niosomes for promotion

of antitumor and antimicrobial photodynamic therapy. J Drug Deliv Sci Tec 2022;68:103031.
[7] Saczko J, Choromanska A, Rembialkowska N, Dubinska-Magiera M, Bednarz-Misa I, Bar J, et al. Oxidative modification induced by photodynamic therapy with Photofrin® II and 2-methoxyestradiol in human ovarian clear carcinoma (OvBH-1) and human breast adenocarcinoma (MCF-7) cells. Biomed Pharmacother 2015;71:30–6.
[8] Swamy PCA, Sivaraman G, Priyanka RN, Raja SO, Ponnuvel K, Shanmugpriya J, et al. Near infrared (NIR) absorbing dyes as promising photosensitizer for photo dynamic therapy. Coordin Chem Rev 2020;411:213233.
[9] Wang KN, Liu LY, Mao D, Hou MX, Tan CP, Mao ZW, et al. A nuclear-targeted AIE photosensitizer for enzyme inhibition and photosensitization in cancer cell ablation. Angew Chem Int Edit 2022;61:e202114600.
[10] Chen C, Wu C, Yu J, Zhu X, Wu Y, Liu J, et al. Photodynamic-based combinatorial cancer therapy strategies: tuning the properties of nanoplatform according to oncotherapy needs. Coordin Chem Rev 2022;461:214495.
[11] Zhou Z, Song J, Nie L, Chen X. Reactive oxygen species generating systems meeting challenges of photodynamic cancer therapy. Chem Soc Rev 2016;45:6597–626.
[12] Wei F, Rees TW, Liao X, Ji L, Chao H. Oxygen self-sufficient photodynamic therapy. Coordin Chem Rev 2021;432:213714.
[13] Yang H, Liu R, Xu Y, Qian L, Dai Z. Photosensitizer nanoparticles boost photodynamic therapy for pancreatic cancer treatment. Nano-Micro Lett 2021;13:35.
[14] Zhang D, Teng KX, Zhao LY, Niu LY, Yang QZ. Ultra-small nano-assemblies as tumor-targeted and renal clearable theranostic agent for photodynamic therapy. Adv Mater 2023;35:2209789.
[15] Zhao X, Liu J, Fan J, Chao H, Peng X. Recent progress in photosensitizers for overcoming the challenges of photodynamic therapy: from molecular design to application. Chem Soc Rev 2021;50:4185–219.
[16] Zheng L, Zhu Y, Sun Y, Xia S, Duan S, Yu B, et al. Flexible modulation of cellular activities with cationic photosensitizers: insights of alkyl chain length on reactive oxygen species antimicrobial mechanisms. Adv Mater 2023;35:2302943.
[17] Zhou Z, Zhang L, Zhang Z, Liu Z. Advances in photosensitizer-related design for photodynamic therapy. Asian J Pharm Sci 2021;16:668–86.
[18] Liu T, Chen Y, Wang H, Cui M, Zhang J, Zhang W, et al. Phototheranostic agents based on nonionic heptamethine cyanine for realizing synergistic cancer phototherapy. Adv Healthc Mater 2023;12:2202817.
[19] Tian H, Zhou L, Wang Y, Nice EC, Huang C, Zhang H. A targeted nanomodulator capable of manipulating tumor microenvironment against metastasis. J Control Release 2022;348:590–600.
[20] Wang SZ, Guo Y, Zhang X, Feng HH, Wu SY, Zhu YX, et al. Mitochondria-targeted photodynamic and mild-temperature photothermal therapy for realizing enhanced immunogenic cancer cell death via mitochondrial stress. Adv Funct Mater 2023;33:2303328.
[21] Wang Y, Yue C, Zhang M, Li D, Xu T, He M, et al. Dually enhanced phototherapy by gambogic acid and hyperthemia-activated chemotherapy for synergistic breast cancer treatment. Chem. Eng. J 2023;452:139108.
[22] Zhao X, Yao Q, Long S, Chi W, Yang Y, Tan D, et al. An approach to developing cyanines with simultaneous intersystem crossing enhancement and excited-state lifetime elongation for photodynamic antitumor metastasis. J Am Chem Soc 2021;143:12345–54.
[23] Zhen X, Jia L, Tang Q, Zhao Y, Li P, Li J, et al. Hybrid biointerface engineering nanoplatform for dual-targeted tumor hypoxia relief and enhanced photodynamic therapy. J Colloid Interf Sci 2023;647:211–23.
[24] Feng Z, Yu XM, Jiang MX, Zhu L, Zhang Y, Yang W, et al. Excretable IR-820 for *in vivo* NIR-II fluorescence cerebrovascular imaging and photothermal therapy of subcutaneous tumor. Theranostics 2019;9:5706–19.
[25] Lin QS, Wang YC, Wang LL, Fan ZJ. Engineered macrophage-derived cellular vesicles for NIR-II fluorescence imaging-guided precise cancer photo-immunotherapy. Colloid Surf B 2024;235:113770.
[26] Chen S, Liu J, Li Y, Wu X, Yuan Q, Yang R, et al. Hypoxia-responsive fluorescent nanoprobe for imaging and cancer therapy. Trac-Trend Anal Chem 2020;131:116010.
[27] Kabakov AE, Yakimova AO. Hypoxia-induced cancer cell responses driving radioresistance of hypoxic tumors: approaches to targeting and radiosensitizing. Cancers 2021;13:1102.
[28] Su J, Zhao Q, Zheng Z, Wang H, Bian C, Meng L, et al. Prospective application of ferroptosis in hypoxic cells for tumor radiotherapy. Antioxidants 2022;11:921.
[29] Han X, Li Y, Zhou Y, Song Z, Deng Y, Qin J, et al. Metal-organic frameworks-derived bimetallic nanozyme platform enhances cytotoxic effect of photodynamic therapy in hypoxic cancer cells. Mater Des 2021;204:109646.
[30] Huang L, Zhao S, Wu J, Yu L, Singh N, Yang K, et al. Photodynamic therapy for hypoxic tumors: advances and perspectives. Coordin Chem Rev 2021;438:213888.
[31] Li X, Kwon N, Guo T, Liu Z, Yoon J. Innovative strategies for hypoxic-tumor photodynamic therapy. Angew Chem Int Edit 2018;57:11522–31.
[32] Cong C, He Y, Zhao S, Zhang X, Li L, Wang D, et al. Diagnostic and therapeutic nanoenzymes for enhanced chemo-therapy and photodynamic therapy. J Mater Chem B 2021;9:3925–3934.
[33] Ding B, Shao S, Yu C, Teng B, Wang M, Cheng Z, et al. Large-pore mesoporous-silica-coated upconversion nanoparticles as multifunctional immunoadjuvants with ultrahigh photosensitizer and antigen loading efficiency for improved cancer photodynamic immunotherapy. Adv Mater 2018;30:1802479.
[34] Wang YE, Zhai J, Zheng Y, Pan J, Liu X, Ma Y, et al. Self-assembled iRGD-R7-LAHP-M nanoparticle induced sufficient singlet oxygen and enhanced tumor penetration immunological therapy. Nanoscale 2022;14:11388–406.
[35] Yang Y, Zhang Y, Wang R, Rong X, Liu T, Xia X, et al. A glutathione activatable pro-drug-photosensitizer for combined chemotherapy and photodynamic therapy. Chinese Chem Lett 2022;33:4583–6.
[36] Liu S, Pan X, Liu H. Two-dimensional nanomaterials for photothermal therapy. Angew Chem Int Edit 2020;59:5890–900.
[37] Zhi D, Yang T, O'hagan J, Zhang S, Donnelly RF. Photothermal therapy. J Control Release 2020;325:52–71.
[38] He Y, Guo S, Zhang Y, Liu Y, Ju H. NIR-II reinforced intracellular cyclic reaction to enhance chemodynamic therapy with abundant H_2O_2 supply. Biomaterials 2021;275:120962.
[39] Li Q, Hang L, Jiang W, Dou J, Xiao L, Tang X, et al. Pre-and post-irradiation mild hyperthermia enabled by H_2O_2 for sensitizing radiotherapy. Biomaterials 2020;257:120235.
[40] Song CW, Park HJ, Lee CK, Griffin R. Implications of increased tumor blood flow and oxygenation caused by mild temperature hyperthermia in tumor treatment. Int J Hyperther 2005;21:761–7.
[41] Ma G, Liu Z, Zhu C, Chen H, Kwok RTK, Zhang P, et al. H2o2-responsive nir-ii aie nanobomb for carbon monoxide boosting low-temperature photothermal therapy. Angew Chem Int Edit 2022;61:e202207213.

[42] Wang Z, Li S, Zhang M, Ma Y, Liu Y, Gao W, et al. Laser-triggered small interfering RNA releasing gold nanoshells against heat shock protein for sensitized photothermal therapy. Adv Sci 2017;4:1600327.
[43] Xia Y, Li C, Cao J, Chen Z, Wang J, Wu Y, et al. Liposome-templated gold nanoparticles for precisely temperature-controlled photothermal therapy based on heat shock protein expression. Colloid Surf B 2022;217:112686.
[44] Zhang X, Xue S-S, Pan W, Wang K, Li N, Tang B. A hypoxia-activated photothermal agent inhibits multiple heat shock proteins for low-temperature photothermal therapy. Chem Commun 2023;59:3898–901.
[45] Hou YJ, Yang XX, Liu RQ, Zhao D, Guo CX, Zhu AC, et al. Pathological mechanism of photodynamic therapy and photothermal therapy based on nanoparticles. Int J Nanomed 2020;15:6827–38.
[46] Shi H, Xiong CF, Zhang LJ, Cao HUC, Wang R, Pan P, et al. Light-triggered nitric oxide nanogenerator with high L-arginine loading for synergistic photodynamic/gas/photothermal therapy. Adv Healthc Mater 2023;12:2300012.
[47] Zhang C, Hu X, Jin L, Lin L, Lin H, Yang Z, et al. Strategic design of conquering hypoxia in tumor for advanced photodynamic therapy. Adv Healthc Mater 2023;12:2300530.
[48] Gao D, Shi Y, Ni J, Chen S, Wang Y, Zhao B, et al. NIR/MRI-guided oxygen-independent carrier-free anti-tumor nano-theranostics. Small 2022;18:2106000.
[49] Han N, Shi Q, Wang X, Huang X, Ruan M, Ren L, et al. Liposome co-loaded with beta-elemene and ir780 for combined chemo-phototherapy. J Drug Deliv Sci Tec 2022;68:103122.
[50] Mo Z, Qiu M, Zhao K, Hu H, Xu Q, Cao J, et al. Multifunctional phototheranostic nanoplatform based on polydopamine-manganese dioxide-ir780 iodide for effective magnetic resonance imaging-guided synergistic photodynamic/photothermal therapy. J Colloid Interf Sci 2022;611:193–204.
[51] Weng S, Pan L, Jiang D, Xie W, Zhang Z, Shi C, et al. Idarubicin and IR780 co-loaded PEG-b-PTMC nanoparticle for non-Hodgkin's lymphoma therapy by photothermal/photodynamic strategy. Mater Des 2023;230:112008.
[52] Wu N, Tu Y, Fan G, Ding J, Luo J, Wang W, et al. Enhanced photodynamic therapy/photothermo therapy for nasopharyngeal carcinoma via a tumour microenvironment-responsive self-oxygenated drug delivery system. Asian J Pharm Sci 2022;17:253–67.
[53] Nani RR, Gorka AP, Nagaya T, Yamamoto T, Ivanic J, Kobayashi H, et al. *In vivo* activation of duocarmycin-antibody conjugates by near-infrared light. Acs Cent Sci 2017;3:329–37.
[54] Nani RR, Kelley JA, Ivanic J, Schnermann MJ. Reactive species involved in the regioselective photooxidation of heptamethine cyanines. Chem Sci 2015;6:6556–63.
[55] Yang G, Tian J, Chen C, Jiang D, Xue Y, Wang C, et al. An oxygen self-sufficient nir-responsive nanosystem for enhanced pdt and chemotherapy against hypoxic tumors. Chem Sci 2019;10:5766–72.
[56] Lei Z, Li X, Luo X, He H, Zheng J, Qian X, et al. Bright, stable, and biocompatible organic fluorophores absorbing/emitting in the deep near-infrared spectral region. Angew Chem Int Edit 2017;56:2979–83.
[57] Hu J, Wang G, Zhao W, Liu X, Zhang L, Gao W. Site-specific *in situ* growth of an interferon-polymer conjugate that outperforms PEGASYS in cancer therapy. Biomaterials 2016;96:84–92.
[58] Liu F, Wang D, Zhang M, Ma L, Yu C, Wei H. Synthesis of enzyme-responsive theranostic amphiphilic conjugated bottlebrush copolymers for enhanced anticancer drug delivery. Acta Biomater 2022;144:15–31.